JACS
JOURNAL OF THE AMERICAN CHEMICAL SOCIETY

Article

pubs.acs.org/JACS

Engineering Interfacial Charge Transfer in $CsPbBr_3$ Perovskite Nanocrystals by Heterovalent Doping

Raihana Begum,[†,§] Manas R. Parida,[†,§] Ahmed L. Abdelhady,[†] Banavoth Murali,[†] Noktan M. Alyami,[†] Ghada H. Ahmed,[†] Mohamed Nejib Hedhili,[‡] Osman M. Bakr,*[,†] and Omar F. Mohammed*[,†]

[†]KAUST Solar Center, Division of Physical Sciences and Engineering and [‡]Imaging and Characterization Laboratory, King Abdullah University of Science and Technology (KAUST), Thuwal 23955-6900, Kingdom of Saudi Arabia

Supporting Information

ABSTRACT: Since compelling device efficiencies of perovskite solar cells have been achieved, investigative efforts have turned to understand other key challenges in these systems, such as engineering interfacial energy-level alignment and charge transfer (CT). However, these types of studies on perovskite thin-film devices are impeded by the morphological and compositional heterogeneity of the films and their ill-defined surfaces. Here, we use well-defined ligand-protected perovskite nanocrystals (NCs) as model systems to elucidate the role of heterovalent doping on charge-carrier dynamics and energy level alignment at the interface of perovskite NCs with molecular acceptors. More specifically, we develop an in situ doping approach for colloidal $CsPbBr_3$ perovskite NCs with heterovalent Bi^{3+} ions by hot injection to precisely tune their band structure and excited-state dynamics. This synthetic method allowed us to map the impact of doping on CT from the NCs to different molecular acceptors. Using time-resolved spectroscopy with broadband capability, we clearly demonstrate that CT at the interface of NCs can be tuned and promoted by metal ion doping. We found that doping increases the energy difference between states of the molecular acceptor and the donor moieties, subsequently facilitating the interfacial CT process. This work highlights the key variable components not only for promoting interfacial CT in perovskites, but also for establishing a higher degree of precision and control over the surface and the interface of perovskite molecular acceptors.

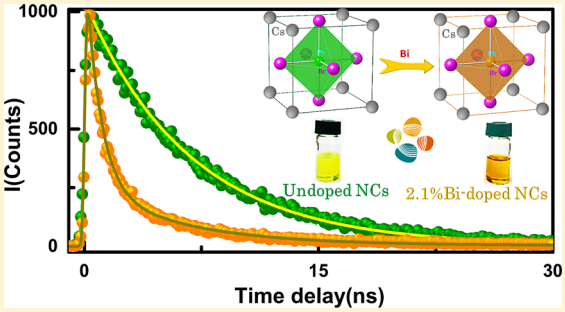

INTRODUCTION

Perovskite nanocrystals (NCs) are promising materials for display devices, visible-light communication systems, lasers, and light-emitting diodes (LEDs).[1−4] Their optical and electronic properties are easily tunable by adjusting their size, composition, and dimensionality.[5−10] Moreover, their defined structure, composition, and ligand-protected surfaces make them unique model systems for investigating some of the most perplexing challenges hampering the advancement of bulk perovskite-based devices. Since achieving milestones in device efficiencies, efforts to improve bulk perovskite-based optoelectronics, such as solar cells and photodetectors, have shifted to other central challenges, such as establishing stability and engineering charge transfer (CT) at interfaces (e.g., through doping).[11] The latter is difficult to investigate in perovskite-based thin film devices because they suffer from ill-defined surfaces and morphologies, and because they have broad variations in their compositions (grain-to-grain).[12]

It is well documented that doping generally leads to new optical, magnetic, and electrical properties.[13,14] Heterovalent metal doping leads to significant changes in the conductivity, as in the case of chalcogenide and pnictogenide binary NCs and bulk metal-halide perovskites.[11,15−18] To date, the potential role of heterovalent-metal doping on the charge transfer and energy-level alignment at the interfaces of metal-halide perovskite NCs remains unknown. Thus far, only isovalent doping in NCs has been reported.[19] Here, we were thus motivated to design a synthetic method for the in situ heterovalent-metal doping of $CsPbBr_3$ perovskite NCs. We developed a hot-injection approach to dope perovskite NCs with Bi^{3+}, while preserving the crystal structure of the host. This method allowed us to reveal heterovalent-metal doping as a tool for modulating interfacial CT and energy-level alignment in NCs. Our time-resolved photoluminescence (PL) and transient-absorption (TA) studies demonstrate that the dopants not only introduce significant changes in the band gaps of the perovskite NCs, but also facilitate CT at the interface of these NCs with different molecular acceptors, including tetracyanoethylene (TCNE) and phenyl-C_{61}-butyric acid methyl ester ($PC_{61}BM$).

EXPERIMENTAL SECTION

Synthesis of Undoped and Doped NCs. Both Bi-doped and undoped $CsPbBr_3$ NCs were synthesized following the hot-injection method reported by Protesescu et al.[20] with some modifications. Cesium oleate (Cs-oleate) was prepared by reacting cesium carbonate (0.203 g) with oleic acid (650 μL) in octadecene (10 mL) solvent. The reaction was maintained under vacuum conditions with continuous

Received: September 12, 2016
Published: December 15, 2016

DOI: 10.1021/jacs.6b09575
J. Am. Chem. Soc. 2017, 139, 731−737

stirring at 120 °C for 1 h followed by purging of N_2 gas until all solute had completely dissolved. Next, $PbBr_2$ (0.069 g) and octadecene (5 mL) were loaded in a two-neck flask and maintained under vacuum conditions for about 30 min at 120 °C. This was followed by addition of oleic acid (1 mL) and oleylamine (550 μL). After complete dissolution of the precursor, the vacuum was stopped and the temperature was raised to 165 °C while purging N_2 gas. The Cs-oleate (400 μL) prepared in the step above was then injected into the contents of the two-necked flask, which was immediately transferred to an ice−water bath. The $CsPbBr_3$ NCs that formed in the octadecene were centrifuged at 5000 rpm for 5 min and the supernatant was discarded. The pellet was dispersed in toluene, washed twice with acetonitrile, and then centrifuged again at 7000 rpm for 5 min. The resultant NCs were redispersed in toluene for a second time and centrifuged again at higher speed to discard the bigger particles. The NCs were doped by adding three concentrations of $BiBr_3$ and $PbBr_2$. Cs-oleate was injected at comparatively lower temperature (165 °C) to avoid surface adsorption of the dopants.

Characterization. *UV−Vis Absorption and PL Spectra.* Spectra of freshly prepared $CsPbBr_3$ NCs doped and undoped redispersed in toluene were obtained using a Cary-5000 spectrophotometer from Agilent Technologies and a FluoroMax-4 spectrofluorometer from Horiba Scientific.

Powder X-ray Diffraction (XRD). Patterns were recorded in thin film mode on a Bruker AXS D8 diffractometer using Cu Kα radiation (λ = 1.54178 Å).

Transmission Electron Microscopy (TEM). Data were obtained using a Titan transmission electron microscope (FEI Company) operating at a beam energy of 300 keV and equipped with a Tridiem postcolumn energy filter (Gatan, IQD). The samples were imaged in EFTEM mode with a 20 eV energy slit inserted around the zero-energy loss of electrons to acquire high-resolution TEM (HRTEM) micrographs.

Photoemission Spectroscopy in Air (PESA). Measurements were carried out using a Riken photoelectron spectrometer (model AC-2) with an ultraviolet (UV) lamp at an intensity of 50 nW. PESA was used to measure the yield of photoemitted electrons (cube root of Yield) being ejected from the sample as a function of photon energy.

Samples of doped and undoped NCs redispersed in toluene were drop cast on glass for XRD and indium tin oxide (ITO) glass substrates for PESA measurements. Samples were dried at room temperature and measurements were performed under ambient conditions. Samples were prepared similarly for TEM measurements with the exception of drop casting on carbon-coated copper grids.

Trace-Metal Analysis. Analysis was carried out using inductively coupled plasma optical emission spectrometry (ICP-OES) on a Varian 720-ES ICP-optical emission spectrometer. Dried powdered samples of NCs were first acid digested in a microwave and then diluted prior to measurements. ICP-OES measurements with a detection limit ranging from parts per million (ppm) to parts per billion (ppb) were performed twice on separately synthesized NC samples (synthesized under identical reaction conditions) and standard deviations were calculated accordingly.

Kelvin Probe. Probe (from KP Technology, KP software 9.1) measurement was done in a glovebox. NC samples were drop cast on ITO glass substrates. A gold test sample was used as a reference. The Kelvin probe measured the energy difference between the work function of the sample and that of the reference metal plate.

X-ray Photoelectron Spectroscopy (XPS). Measurements were carried out in a Kratos Axis Ultra DLD spectrometer equipped with a monochromatic Al Kα X-ray source ($h\nu$ = 1486.6 eV) operating at 150 W, a multichannel plate, and a delay line detector under 1.0×10^{-9} Torr vacuum. The survey and the high-resolution spectra were collected at fixed analyzer pass energies of 160 and 20 eV, respectively. Measurements were performed on NCs samples dispersed in toluene drop cast on a glass substrate. Note that charge neutralization was required for these measurements. Binding energies were referenced to the C 1s peak (set at 284.8 eV) of the sp^3 hybridized (C−C) carbon (from oleylamine and oleic acid present in the NCs). The data were analyzed with commercially available software, CasaXPS. The individual peaks were fitted by a Gaussian (70%)−Lorentzian (30%) (GL30) function after linear or Shirley-type background subtraction.

Femto- and Nanosecond Transient Absorption. Spectra were collected using an ultrafast Systems Helios and EOS spectrometers with broadband capability and time resolutions of 120 fs and 800 ps, respectively. The probe pulse was generated in a 2 mm thick calcium floride (CaF_2) plate in the Helios spectrometer using a few microjoules of pulse energy from the fundamental output of a Ti:sapphire femtosecond regenerative amplifier operating at 800 nm with 35 fs pulses and a repetition rate of 1 kHz. In EOS experiments, the white-light continuum probe pulse was generated by a super continuum source instead of CaF_2 crystal used in Helios. A two-channel probe (probe-reference) method was used for both spectrometers. This method splits the probe beam into two before passing through the sample. While one arm travels through the sample, the other is sent directly to the reference spectrometer that monitors the fluctuations in the probe beam intensity. The main advantage of this technique is that it allows the user to achieve the specified signal-to-noise ratio with a lower number of averaged laser pulses. The pump pulses at 370 nm were created from spectrally tunable (240−2600 nm) femtosecond pulses generated in the optical parametric amplifier (Newport Spectra-Physics). Finally, pump and probe beams were focused on the sample solution, and the transmitted probe light from the samples was collected and focused on the broadband UV−visible detector to record the time-resolved transient absorption spectra.

RESULTS AND DISCUSSION

Oleic acid capped $CsPbBr_3$ perovskite NCs were synthesized following a well-established method[20] with minor modifications as represented in Scheme S1 (see the Supporting Information, SI). Three concentrations of bismuth bromide (2%, 5%, and 10%) with respect to lead bromide were used during synthesis. An optimal concentration of oleic acid and oleylamine was used to facilitate the solubilization of the Pb^{2+} and Bi^{3+} precursors as reported perviously.[21] The NCs were size-selectively precipitated by centrifugation at different speeds to ensure a narrow size distribution. Finally, they were redispersed in toluene for detailed optical characterizations.

We calculated the average size of the cubic-shaped NCs from HRTEM images to be ∼8.7 ± 0.2 nm (Figures 1A, B, and S1, S2, SI). The results indicate that the Bi-doped and undoped NCs had the same particle size and shape. We also used these images to calculate the interplanar distance (d = 0.58 nm) of doped and undoped NCs. The Bragg reflections in powder XRD patterns (Figure S3) were consistent with results published in the literature.[22] As shown in Figure S3, the peak positions of the XRD patterns did not shift upon doping.

We performed several experiments confirming the successful incorporation of Bi^{3+} into the NCs. Figure S4 illustrates XPS results revealing that both Bi-doped and undoped NCs comprised Cs, Pb, Br, C, N, and O, consistent with the literature.[23] High-resolution spectra corresponding to the core levels of Cs 3d, Cs 4P, Pb 4f, and Br 3d were recorded. Although the peak positions for both doped and undoped NCs were the same, we observed an additional peak from Bi-doped NCs at 164.4 eV, which we attributed to the Bi $4f_{5/2}$ component of Bi^{3+}.[24] Another component of the Bi 4f core level, Bi $4f_{7/2}$, was difficult to distinguish because it overlapped with Cs ($4P_{3/2}$) at 158.9 eV, as shown in Figure S4b. It also coincided with the corresponding doublet of Cs ($4P_{1/2}$) located at 170.3 eV. We substantiated these XPS findings with results from ICP-OES, which clearly indicated that the ratio of Bi/Pb increased monotonically as the concentration of bismuth bromide was increased in the feed solution (Figure S5). Note that the amount of Bi decreased after the NCs were washed a

DOI: 10.1021/jacs.6b09575
J. Am. Chem. Soc. 2017, 139, 731−737

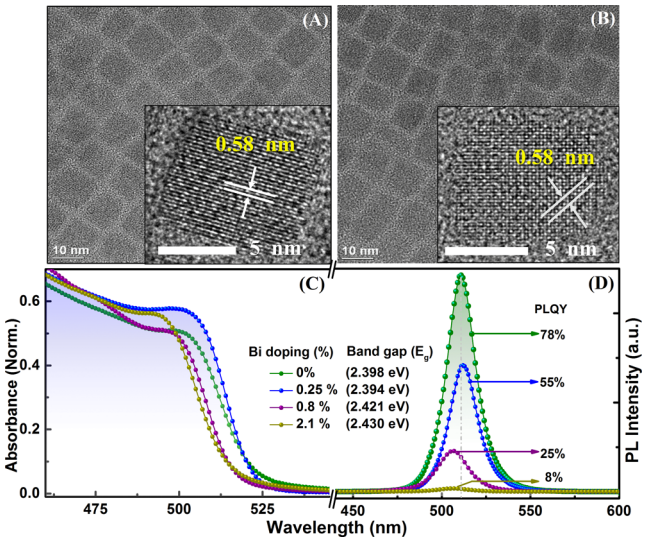

Figure 1. TEM images of $CsPbBr_3$ NCs (A) undoped, (B) 2.1% Bi^{3+}-doped, with HRTEM images shown in the insets, indicating no change in average size, shape, or crystal structure upon doping. (C) Absorption and (D) PL spectra (λ_{ex} = 365 nm) of undoped and Bi-doped (0.25%, 0.8%, and 2.1%) $CsPbBr_3$ NCs showing the spectral shift and change in the band gap energy, E_g (calculated from a Tauc plot).

second time with acetonitrile, suggesting that initially some loosely bonded or surface-adsorbed Bi atoms were on the doped NCs. A third wash of the NCs, however, did not significantly change the dopant content, indicating that the dopant was present in the core of the NCs. It should be noted that we were unable to identify the exact location of the dopant by X-ray absorption spectroscopy (XAS) due to the similar atomic emission features of Bi and Pb.[25] In the 2%, 5%, and 10% Bi concentrations, the actual concentration in the NCs (after the second wash) was estimated to be 0.25%, 0.8%, and 2.1%, respectively. We also calculated the average amount of Bi per NC (listed in Tables S1 and S2) and plotted the Bi atoms incorporated in each NC, as determined by ICP-OES in relation to the Bi/NC ratio in the feed solution (Figure S6). The highest doping level achieved in our experiments can be considered to be likened to the heavy doping described in the literature.[18,26] The in situ hot-injection method yielded 19% doping (calculated from the slope of the curve in Figure S6) in the NCs that were used for spectroscopic measurements.

Next, we compared the steady state absorption and PL spectra of Bi-doped and undoped $CsPbBr_3$ NCs as shown in Figures 1C and D. As can be seen, the first excitonic peak shifted to a lower energy when doped with lower concentration (Bi/Pb = 0.25%) and then it shifted to a higher energy at high doping levels, providing another piece of evidence for the successful incorporation of Bi^{3+} into the core of the NCs. An absence of Urbach tailing in our doped NCs suggested that there was no lattice distortion upon doping unlike that occurs in Bi-doped halide perovskite single crystals.[11] It is worth highlighting that the absence of any tailing in the absorption spectrum upon doping is beneficial as a sharp absorption edge which is a merit of halide perovskites.[27] Optical band gaps were quantified from the Tauc plot of $(\alpha h\nu)^2$ versus $h\nu$, which illustrates the band gaps of undoped and Bi-doped NCs (Figure S7). Undoped $CsPbBr_3$ NCs showed a band gap of 2.39 eV, consistent with that previously reported.[28] However, the plot of the energy shift (ΔE) of the first exciton peak in relation to the Bi/NC ratio (estimated by ICP), shown in Figure S8, further confirms the incorporation of Bi^{3+} in the crystal lattice. A similar trend due to n-type doping has previously been reported in Cu-doped InAs NC.[26] Finally, we used Kelvin-probe measurements for undoped and Bi-doped NCs to determine the position of the Fermi level (see Figure S9). The Fermi level (E_F) of undoped $CsPbBr_3$ NCs was close to the valence band edge. Meanwhile, as Bi content increased, the Fermi level gradually shifted toward the conduction band edge, further confirmed the presence of Bi doping in the crystal lattice.

As can be seen in the PL spectra of the NCs samples in Figure 1D, a nominal red shift is followed by a blue shift from 517 to 512 nm at higher Bi/Pb ratios. It is widely accepted that as dopant content increases, impurity levels interact with each other to form a bandlike structure within the band gap of the host[18] (Figure 2). We attribute the observed spectral shift to

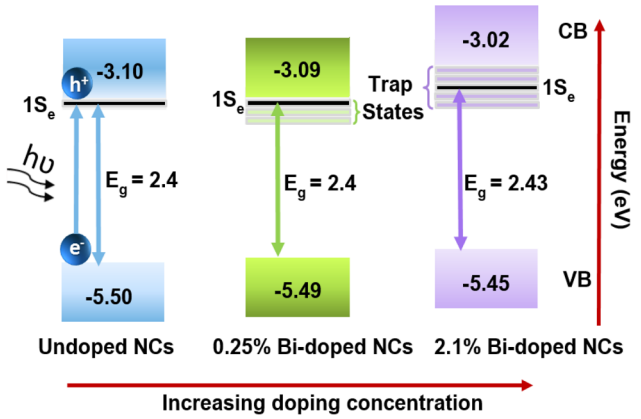

Figure 2. Schematic representation showing changes in the band alignments of $CsPbBr_3$ NCs upon doping with 0.25 or 2.1% Bi. We measured the E_V of NCs by PESA (Figure S14), and E_C is estimated by subtracting the band gap energy (calculated from the Tauc Plot) from the respective E_V values; (E_V and E_C are the valence and conduction band energies, respectively).

filling of the conduction band with extra electrons donated by the dopants, also known as the Burstein–Moss effect.[29] At low doping concentrations, a red shift arises with fewer impurity levels or trap states "below" the first electronic state, $1S_e$, of the conduction band. At high-doping concentrations, a blue shift is observed due to the evolution of the trap states "above" the $1S_e$ state (Figure 2). A similar result has been reported for Cu-doped InAs NCs.[26] Note that the full width at half-maximum of the emission peak in all samples was between 18 and 21 nm, which is indicative of a narrow particle size distribution (see Figure 1). Moreover, we observed that the emission intensity monotonically decreased with dopant concentration as was previously reported for Bi-doped PbS quantum dots.[24] The quantum yield for undoped $CsPbBr_3$ NCs was found to be 78% and it decreased to 8% at high-doping concentration (Bi/Pb = 2.1%). This decrease in emission intensity suggests that Bi atoms may have been incorporated into the $CsPbBr_3$ host lattice, causing strong perturbation to the density of states.[18,24,30]

To explore the impact of doping on the carrier lifetime and the deactivation of the excited carriers, we performed time-resolved PL and nanosecond transient absorption spectroscopy, respectively. The experimental setups of our PL and TA

DOI: 10.1021/jacs.6b09575
J. Am. Chem. Soc. 2017, 139, 731–737

spectroscopies have previously been described.[31−33] Optical excitation with 370 nm laser pulses caused ground-state bleaching (GSB) at 506 and 499 nm for undoped and doped NCs, respectively (as shown in Figure 3A and B).

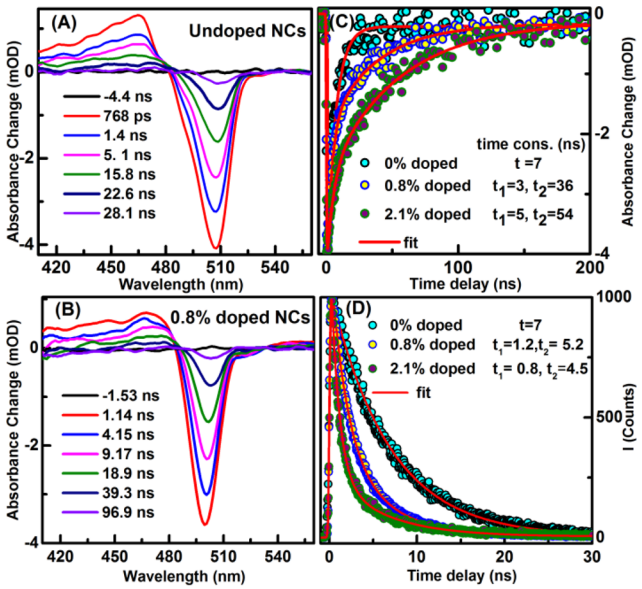

Figure 3. ns-TA spectra at indicated delay times after 370 nm optical excitation of (A) $CsPbBr_3$ NCs (GSB ∼ 506 nm) and (B) 0.8% Bi-doped $CsPbBr_3$ NCs (GSB ∼ 499 nm) in toluene. (C) Transient kinetic traces as a function of time-delay and (D) time-resolved PL decays for excitation at 370 nm at three doping levels (0%, 0.8%, and 2.1%).

The spectral changes in the TA of Bi-doped $CsPbBr_3$ NCs could be attributed to a strong perturbation in the electronic structure that occurs when Bi-dopant atoms are introduced into the $CsPbBr_3$ NC structure.[34] We followed the GSB recovery to study the charge carrier recombination dynamics. The GSB centered at 506 nm in undoped $CsPbBr_3$ NCs revealed full recovery with a time constant of 7 ns, while in 0.8% doped NCs, the GSB showed full recovery with a time constant of 36 ns (Figure 3C). Fitting of the kinetic profiles of 0.8% Bi-doped $CsPbBr_3$ NCs showed two lifetime components, a fast component of 3 ns and a long component of 36 ns, while undoped $CsPbBr_3$ NCs showed just a single dominant lifetime. As can be seen in Figure 3C, a greater increase in the long component of charge recombination time was observed in 2.1% Bi-doped $CsPbBr_3$ NCs. This implies the involvement of change in the electronic band structure which delays carrier recombination in Bi-doped NCs.[35] Time-resolved PL decay measurements complement these results, as shown in Figure 3D, whereby undoped NCs showed exponential decay with a lifetime of 7 ns, results in agreement with a recent report.[36] Noted that perovskite NCs are known to have much shorter PL lifetimes than bulk single crystals due to the stronger overlap between electron−hole wave functions in a spatially confined space.[36] Meanwhile, the doped NCs exhibited biexponential decay with two lifetime components as presented in Figure 3D. The longer lifetime decreased to 5.2 ns and 4.5 ns for 0.8% and 2.1% doped NCs, respectively. The emission quenching accompanied by a decrease in the PL decay lifetime in Bi-doped $CsPbBr_3$ NCs further substantiated the presence of trap states in the band gap of the host $CsPbBr_3$ NCs upon doping with Bi. Such trap states provide alternative ways for electronic relaxation and consequently reduce radiative recombination.

To understand the impact of doping on the CT at the interface of these NCs with molecular acceptors, so we can take the work an important step further, we performed femtosecond transient absorption (fs)-TA spectroscopy with broadband capability on undoped and doped NCs in the presence of TCNE, a known electron acceptor.

As TCNE was successively added (0.1 mM to 0.8 mM) to doped and undoped $CsPbBr_3$ NCs, we observed a gradual decrease in emission intensity, as shown in Figure S10. We observed maximum quenching of about 90% for 0.8% doped NCs and 78% for undoped NCs under the same experimental conditions. Although this degree of exciton quenching could also be a consequence of energy transfer, we excluded this possibility due to the lack of spectral overlap between the absorption of TCNE and the emission of NCs, as shown in Figure S11. TEM images show that treatment with TCNE (inset, Figure S10) did not change the size or shape of the NCs. With the addition of TCNE, we observed a red shift of 5−8 nm in the absorption spectra of both undoped and doped NCs and a concomitant red shift in the position of the PL emission maximum. These changes in the absorption and PL spectra of the NCs upon addition of TCNE indicate the formation of a ground-state complex between the donor and acceptor. Such a strong electronic coupling between TCNE and the excited state of the NCs might facilitate the photoinduced electron transfer from NCs to TCNE.[37] To understand the mechanism of the photoinduced electron transfer, we analyzed the PL data using the Stern−Volmer equation.[38] From the plot shown in Figure S12, we estimated quenching rates at 9.1×10^{12} $M^{-1}S^{1-}$ and 7.1×10^{12} $M^{-1}S^{1-}$ for 0.8% doped and undoped NCs, respectively. These rates suggest that the quenching mechanism is static in nature (also, supported by fs-TA measurements).

Figure 4 shows the fs-TA spectra and corresponding transient kinetic traces of undoped and 0.8%-doped samples with and without TCNE molecular acceptors. In the presence of TCNE, GSB is slightly red-shifted, similar to what we observed in the steady-state absorption spectra (Figure S10). GSB occurs due to filling of 1S levels of the conduction band by excited electrons and recovery occurs when the electrons are removed or the charge carriers recombine.[39,40] This shift in the position of GSB in the presence of a molecular acceptor may be explained in terms of change in the electron density upon the formation of a ground-state complex. In addition, the recovery of the GSB is ultrafast when coupled with TCNE, regardless of whether NCs were doped or undoped. These results suggest that TCNE provides an additional deactivation channel for the transfer of photogenerated electrons, accelerating recovery (see Figure 4C and D). We also observed that GSB recovery was faster for Bi-doped than for undoped NCs in the presence of TCNE (Figure 4C and D). To obtain a quantitative picture of the carrier dynamics in these NCs, we compared the fs-TA kinetics of undoped and Bi-doped NCs with and without TCNE, as shown in the insets of Figure 4. The kinetics data are fitted with a biexponential function and the acquired time components are presented in Table S3. Both the undoped and 0.8% Bi-doped NCs have one fast component with time constants of about 82 and 128 ps, respectively, and one slow component with a few nanosecond time constant. The fast component may arise from charge-carrier trapping, whereas the slow component can be attributed to excitonic recombination in the NCs.[37,41] We continued to observe both components

DOI: 10.1021/jacs.6b09575
J. Am. Chem. Soc. 2017, 139, 731−737

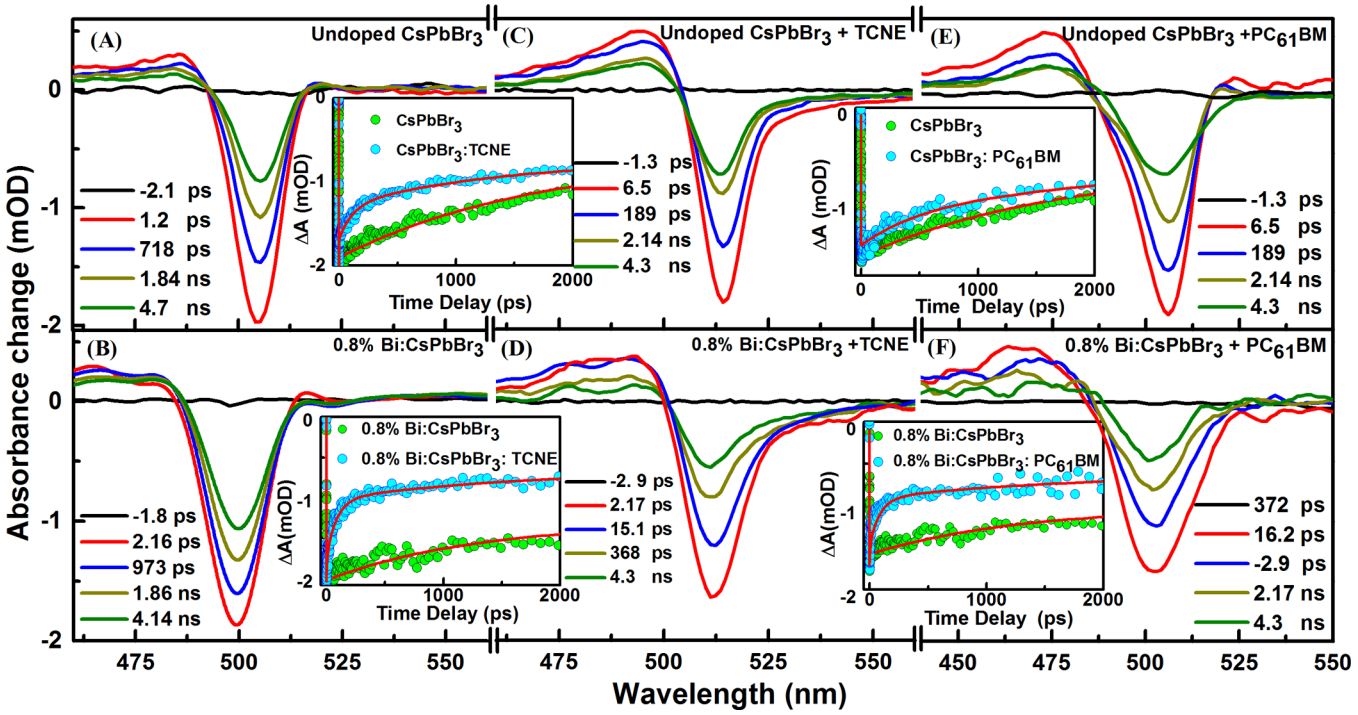

Figure 4. fs-TA spectra at indicated delay times after 370 nm optical excitation of (A) $CsPbBr_3$ NCs, (B) 0.8%-doped $CsPbBr_3$ NCs; (C) and (D) are the same samples in (A) and (B), respectively, treated with 0.8 mM TCNE. Inset figures between (A) and (C), and between (B) and (D) show comparison fs-transient kinetics traces at the respective GSB maxima of the NC samples in the presence and absence of TCNE. (E, F) fs-TA spectra of the undoped and 0.8%-doped NCs treated with 3.5 mM $PC_{61}BM$. Inset figures (right panel) show comparison of fs-transient kinetics traces at the respective GSB maxima of the NC samples in the presence and absence of $PC_{61}BM$. The solid red lines in the insets represent the best fit for the kinetic traces.

after adding TCNE, however, the short component became much faster and the ratio between the fast and slow components increased significantly, reconfirming that TCNE provides an additional channel for fast electron transfer from these NCs. The faster rate of GSB recovery for doped than for undoped NCs indicates that doping increases the rate of CT. We also studied the excited-state dynamics of the undoped and doped NCs in the presence of $PC_{61}BM$ using fs-TA. The steady-state and time-resolved results are shown in Figures S13 and 4E and F. As the concentration of $PC_{61}BM$ was increased from 0.25 mM to 3.5 mM, the emission intensity of the NCs decreased (see Figure S13). Here, we used two-photon excitations at 800 nm to selectively excite the NCs.

The fs-TA spectra of undoped and Bi-doped samples with $PC_{61}BM$ is shown in Figure 4E and F, at two photon laser excitation (at 800 nm). The insets illustrate the fs-TA kinetics traces at the respective GSB positions (right panel of Figure 4). Upon addition of $PC_{61}BM$, we observed faster GSB kinetics of NCs. The faster bleach recovery observed upon coupling with a molecular acceptor was due to electron injection from the conduction band of NCs to the lowest-unoccupied molecular orbital (LUMO) of the acceptor. This offset of the favorable band energy facilitates the electron transfer. The electron transfer rate was found to be relatively higher for 0.8% doped $CsPbBr_3$ NCs than for undoped $CsPbBr_3$ NCs, similar to what we observed in the presence and absence of TCNE.

To gain a new physical insight into the mechanism of the electron injection from Bi-doped and undoped NCs to the two acceptors (TCNE and $PC_{61}BM$), we deciphered the band alignment between the NCs and the molecular acceptor.[42,43] First, we measured the valence band edge (E_V) of the NCs by PESA.[44] We found that E_V = −5.5 and −5.45 eV for undoped and 0.8% Bi-doped NCs, respectively (Figure S14). Similar to that reported in the literature, LUMO values were −3.77 and −3.9 eV for TCNE and $PC_{61}BM$, respectively).[45−47] The band-edge alignment is schematically demonstrated in Scheme 1.

Scheme 1. Band gap offset of undoped and Bi-doped $CsPbBr_3$ NCs with respect to the LUMO of TCNE

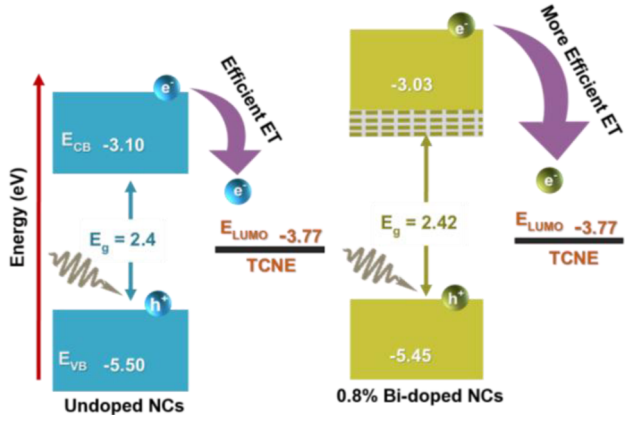

According to Marcus theory, as it correlates with Gibbs free energy (−ΔG), which is the energy difference between the acceptor and donor moieties with the rate of electron transfer, the rate of electron transfer increases as the difference in energy increases.[37,48,49] We observed a clear difference in electron affinities between doped and undoped NCs and both the acceptors. The energy offset between the conduction band of

DOI: 10.1021/jacs.6b09575
J. Am. Chem. Soc. 2017, 139, 731−737

the NCs and both of the molecular acceptors was higher for the Bi-doped NCs than for undoped NCs, thus accelerating the electron injection process.

SUMMARY

In summary, we report the doping of heterovalent Bi^{3+} ions in colloidal $CsPbBr_3$ perovskite NCs by a hot-injection method to tune their electronic structure. We probed the effects of Bi^{3+} doping not only on the band structure and carrier dynamics of $CsPbBr_3$ NCs, but also on the interfacial CT with two well-known molecular acceptors. The fs-TA results clearly show that interfacial CT in this system can be tuned and facilitated by metal doping. This is due to the increase in the driving-force Gibbs free energy ($-\Delta G$) between the molecular acceptor and donor moieties upon metal doping, which leads to more efficient CT from the NCs to molecular acceptors. This novel finding provides a tool to precisely control the CT process at the interface of this promising class of NCs and paves the way for engineering interfacial charge transfer in bulk perovskite devices by heterovalent doping.

ASSOCIATED CONTENT

Supporting Information

The Supporting Information is available free of charge on the ACS Publications website at DOI: 10.1021/jacs.6b09575.

Schematic of in situ doping of perovskite NCs using hot injection; TEM images; particle size distribution; XRD, XPS, PESA, absorption and emission spectra; calculation of Bi atoms/nanocrystal; quantum yield measurements (PDF)

AUTHOR INFORMATION

Corresponding Authors

*osman.bakr@kaust.edu.sa

*omar.abdelsaboor@kaust.edu.sa

ORCID

Banavoth Murali: 0000-0002-7806-2274

Osman M. Bakr: 0000-0002-3428-1002

Omar F. Mohammed: 0000-0001-8500-1130

Author Contributions

§R.B and M.R.P contributed equally to the work.

Notes

The authors declare no competing financial interest.

ACKNOWLEDGMENTS

This work was supported by King Abdullah University of Science and Technology (KAUST). Also, part of this work was supported by a Saudi Arabia Basic Industries Corporation (SABIC) Grant RGC/3/2470-01.

REFERENCES

(1) Yakunin, S.; Protesescu, L.; Krieg, F.; Bodnarchuk, M. I.; Nedelcu, G.; Humer, M.; De Luca, G.; Fiebig, M.; Heiss, W.; Kovalenko, M. V. *Nat. Commun.* **2015**, *6*, 8056.

(2) Pan, J.; Sarmah, S. P.; Murali, B.; Dursun, I.; Peng, W.; Parida, M. R.; Liu, J.; Sinatra, L.; Alyami, N.; Zhao, C.; Alarousu, E.; Ng, T. K.; Ooi, B. S.; Bakr, O. M.; Mohammed, O. F. *J. Phys. Chem. Lett.* **2015**, *6*, 5027−5033.

(3) Li, G.; Rivarola, F. W. R.; Davis, N. J. L. K.; Bai, S.; Jellicoe, T. C.; de la Peña, F.; Hou, S.; Ducati, C.; Gao, F.; Friend, R. H.; Greenham, N. C.; Tan, Z.-K. *Adv. Mater.* **2016**, *28*, 3528−3534.

(4) Dursun, I.; Shen, C.; Parida, M. R.; Pan, J.; Sarmah, S. P.; Priante, D.; Alyami, N.; Liu, J.; Saidaminov, M. I.; Alias, M. S.; Abdelhady, A. L.; Ng, T. K.; Mohammed, O. F.; Ooi, B. S.; Bakr, O. M. *ACS Photonics* **2016**, *3*, 1150−1156.

(5) Nedelcu, G.; Protesescu, L.; Yakunin, S.; Bodnarchuk, M. I.; Grotevent, M. J.; Kovalenko, M. V. *Nano Lett.* **2015**, *15*, 5635−5640.

(6) Sichert, J. A.; Tong, Y.; Mutz, N.; Vollmer, M.; Fischer, S.; Milowska, K. Z.; García Cortadella, R.; Nickel, B.; Cardenas-Daw, C.; Stolarczyk, J. K.; Urban, A. S.; Feldmann, J. *Nano Lett.* **2015**, *15*, 6521−6527.

(7) Huang, H.; Susha, A. S.; Kershaw, S. V.; Hung, T. F.; Rogach, A. L. *Adv. Sci.* **2015**, *2*, 1500194.

(8) Zhang, D.; Yu, Y.; Bekenstein, Y.; Wong, A. B.; Alivisatos, A. P.; Yang, P. *J. Am. Chem. Soc.* **2016**, *138*, 13155−13158.

(9) Zhang, D.; Yang, Y.; Bekenstein, Y.; Yu, Y.; Gibson, N. A.; Wong, A. B.; Eaton, S. W.; Kornienko, N.; Kong, Q.; Lai, M.; Alivisatos, A. P.; Leone, S. R.; Yang, P. *J. Am. Chem. Soc.* **2016**, *138*, 7236−7239.

(10) Akkerman, Q. A.; D'Innocenzo, V.; Accornero, S.; Scarpellini, A.; Petrozza, A.; Prato, M.; Manna, L. *J. Am. Chem. Soc.* **2015**, *137*, 10276−10281.

(11) Abdelhady, A. L.; Saidaminov, M. I.; Murali, B.; Adinolfi, V.; Voznyy, O.; Katsiev, K.; Alarousu, E.; Comin, R.; Dursun, I.; Sinatra, L.; Sargent, E. H.; Mohammed, O. F.; Bakr, O. M. *J. Phys. Chem. Lett.* **2016**, *7*, 295−301.

(12) Li, J.-J.; Ma, J.-Y.; Ge, Q.-Q.; Hu, J.-S.; Wang, D.; Wan, L.-J. *ACS Appl. Mater. Interfaces* **2015**, *7*, 28518−28523.

(13) Begum, R.; Chattopadhyay, A. *J. Phys. Chem. Lett.* **2014**, *5*, 126−130.

(14) Lee, J.-W.; Son, D.-Y.; Ahn, T. K.; Shin, H.-W.; Kim, I. Y.; Hwang, S.-J.; Ko, M. J.; Sul, S.; Han, H.; Park, N.-G. *Sci. Rep.* **2013**, *3*, 1050.

(15) Amit, Y.; Li, Y.; Frenkel, A. I.; Banin, U. *ACS Nano* **2015**, *9*, 10790−10800.

(16) Amit, Y.; Eshet, H.; Faust, A.; Patllola, A.; Rabani, E.; Banin, U.; Frenkel, A. I. *J. Phys. Chem. C* **2013**, *117*, 13688−13696.

(17) Sahu, A.; Kang, M. S.; Kompch, A.; Notthoff, C.; Wills, A. W.; Deng, D.; Winterer, M.; Frisbie, C. D.; Norris, D. J. *Nano Lett.* **2012**, *12*, 2587−2594.

(18) Mocatta, D.; Cohen, G.; Schattner, J.; Millo, O.; Rabani, E.; Banin, U. *Science* **2011**, *332*, 77−81.

(19) Navas, J.; Sanchez-Coronilla, A.; Gallardo, J. J.; Cruz Hernandez, N.; Pinero, J. C.; Alcantara, R.; Fernandez-Lorenzo, C.; De los Santos, D. M.; Aguilar, T.; Martin-Calleja, J. *Nanoscale* **2015**, *7*, 6216−6229.

(20) Protesescu, L.; Yakunin, S.; Bodnarchuk, M. I.; Krieg, F.; Caputo, R.; Hendon, C. H.; Yang, R. X.; Walsh, A.; Kovalenko, M. V. *Nano Lett.* **2015**, *15*, 3692−3696.

(21) De Roo, J.; Ibanez, M.; Geiregat, P.; Nedelcu, G.; Walravens, W.; Maes, J.; Martins, J. C.; Van Driessche, I.; Kovalenko, M. V.; Hens, Z. *ACS Nano* **2016**, *10*, 2071−2081.

(22) Schmidt, L. C.; Pertegas, A.; Gonzalez-Carrero, S.; Malinkiewicz, O.; Agouram, S.; Minguez Espallargas, G.; Bolink, H. J.; Galian, R. E.; Perez-Prieto, J. *J. Am. Chem. Soc.* **2014**, *136*, 850−853.

(23) Sun, S.; Yuan, D.; Xu, Y.; Wang, A.; Deng, Z. *ACS Nano* **2016**, *10*, 3648−3657.

(24) Stavrinadis, A.; Rath, A. K.; de Arquer, F. P.; Diedenhofen, S. L.; Magen, C.; Martinez, L.; So, D.; Konstantatos, G. *Nat. Commun.* **2013**, *4*, 2981.

(25) Stavrinadis, A.; Pelli Cresi, J. S.; d'Acapito, F.; Magén, C.; Boscherini, F.; Konstantatos, G. *Chem. Mater.* **2016**, *28*, 5384−5393.

(26) Yang, C.; Faust, A.; Amit, Y.; Gdor, I.; Banin, U.; Ruhman, S. *J. Phys. Chem. A* **2016**, *120*, 3088−3097.

(27) De Wolf, S.; Holovsky, J.; Moon, S. J.; Loper, P.; Niesen, B.; Ledinsky, M.; Haug, F. J.; Yum, J. H.; Ballif, C. *J. Phys. Chem. Lett.* **2014**, *5*, 1035−1039.

(28) Zhang, X.; Lin, H.; Huang, H.; Reckmeier, C.; Zhang, Y.; Choy, W. C.; Rogach, A. L. *Nano Lett.* **2016**, *16*, 1415−1420.

(29) Kamat, P. V.; Dimitrijevic, N. M.; Nozik, A. J. *J. Phys. Chem.* **1989**, *93*, 2873.

DOI: 10.1021/jacs.6b09575
J. Am. Chem. Soc. 2017, 139, 731−737

(30) Papagiorgis, P.; Stavrinadis, A.; Othonos, A.; Konstantatos, G.; Itskos, G. *Sci. Rep.* **2016**, *6*, 18735.
(31) Soldan, G.; Aljuhani, M. A.; Bootharaju, M. S.; AbdulHalim, L. G.; Parida, M. R.; Emwas, A. H.; Mohammed, O. F.; Bakr, O. M. *Angew. Chem., Int. Ed.* **2016**, *55*, 5749−5753.
(32) El-Ballouli, A. O.; Alarousu, E.; Kirmani, A. R.; Amassian, A.; Bakr, O. M.; Mohammed, O. F. *Adv. Funct. Mater.* **2015**, *25*, 7435−7441.
(33) Aly, S. M.; AbdulHalim, L. G.; Besong, T. M.; Soldan, G.; Bakr, O. M.; Mohammed, O. F. *Nanoscale* **2016**, *8*, 5412−5416.
(34) Jones, M.; Lo, S. S.; Scholes, G. D. *Proc. Natl. Acad. Sci. U. S. A.* **2009**, *106*, 3011−3016.
(35) Koh, W. K.; Koposov, A. Y.; Stewart, J. T.; Pal, B. N.; Robel, I.; Pietryga, J. M.; Klimov, V. I. *Sci. Rep.* **2013**, *3*, 2004.
(36) Hu, F.; Zhang, H.; Sun, C.; Yin, C.; Lv, B.; Zhang, C.; Yu, W.; Wang, F.; Zhang, Y.; Xiao, M. *ACS Nano* **2015**, *9*, 12410−12416.
(37) Ahmed, G. H.; Liu, J.; Parida, M. R.; Murali, B.; Bose, R.; AlYami, N. M.; Hedhili, M. N.; Peng, W.; Pan, J.; Besong, T. M. D.; Bakr, O. M.; Mohammed, O. F. *J. Phys. Chem. Lett.* **2016**, *7*, 3913−3919.
(38) Aly, S. M.; Parida, M. R.; Alarousu, E.; Mohammed, O. F. *Chem. Commun.* **2014**, *50*, 10452−10455.
(39) Song, N.; Zhu, H.; Jin, S.; Zhan, W.; Lian, T. *ACS Nano* **2011**, *5*, 613−621.
(40) Manser, J. S.; Kamat, P. V. *Nat. Photonics* **2014**, *8*, 737−743.
(41) Zhang, F.; Zhong, H.; Chen, C.; Wu, X.-g.; Hu, X.; Huang, H.; Han, J.; Zou, B.; Dong, Y. *ACS Nano* **2015**, *9*, 4533−4542.
(42) Chuang, C. H.; Brown, P. R.; Bulovic, V.; Bawendi, M. G. *Nat. Mater.* **2014**, *13*, 796−801.
(43) Brown, P. R.; Kim, D.; Lunt, R. R.; Zhao, N.; Bawendi, M. G.; Grossman, J. C.; Bulović, V. *ACS Nano* **2014**, *8*, 5863−5872.
(44) Choi, T.; Bedwani, S.; Rochefort, A.; Chen, C.-Y.; Epstein, A. J.; Gupta, J. A. *Nano Lett.* **2010**, *10*, 4175−4180.
(45) Jasieniak, J.; Califano, M.; Watkins, S. E. *ACS Nano* **2011**, *5*, 5888−5902.
(46) Caruso, F.; Atalla, V.; Ren, X.; Rubio, A.; Scheffler, M.; Rinke, P. *Phys. Rev. B: Condens. Matter Mater. Phys.* **2014**, *90*, 085141.
(47) El-Ballouli, A. O.; Alarousu, E.; Bernardi, M.; Aly, S. M.; Lagrow, A. P.; Bakr, O. M.; Mohammed, O. F. *J. Am. Chem. Soc.* **2014**, *136*, 6952−6959.
(48) Olshansky, J. H.; Ding, T. X.; Lee, Y. V.; Leone, S. R.; Alivisatos, A. P. *J. Am. Chem. Soc.* **2015**, *137*, 15567−15575.
(49) Bang, J. H.; Kamat, P. V. *ACS Nano* **2011**, *5*, 9421−9427.

DOI: 10.1021/jacs.6b09575
J. Am. Chem. Soc. 2017, 139, 731−737